A bidirectional power converter connecting electric vehicle battery and DC microgrid

Sulistyo Wijanarko[1,2], Gifari Iswandi Hasyim[1], Jihad Furqani[1], Arwindra Rizqiawan[1], Pekik Argo Dahono[1], Anwar Muqorobin[2]

[1]School of Electrical Engineering and Informatics, Institut Teknologi Bandung, Bandung, Indonesia
[2]Research Center for Energy Conversion and Conservation, National Research and Innovation Agency, South Tangerang, Indonesia

Article Info

ABSTRACT

One way to increase electric vehicle (EV) battery utilization is to connect it to a dc microgrid. The EV battery can assume the role of an energy storage from the grid point of view. A bidirectional DC-DC converter will be needed to transfer power between them back and forth. This paper proposes the converter design considering its functional objective, including interleaved phase number determination. Efficiency performance evaluation is presented by power loss analysis with the parasitic-parameters consideration of the components. Finding optimum switching frequency based on power loss analysis is performed independently between input and output sides of the converter. Finally, experiments using a scaled-down prototype are shown to verify the analytical analysis of the converter. The experimental results properly validate the power loss analytic analysis carried out in this paper with a maximum error of 2.04% at 1131-watt, 60 V battery voltage, and 140 V grid voltage. Maximum efficiency 96.97% is obtained at 301-watt, 130 V battery voltage, and 151 V grid voltage. Overall, the converter has a simple structure, capable to be operated in various levels of input and output voltages with a minimum battery side current ripple.

Corresponding Author:

Sulistyo Wijanarko
Research Center for Energy Conversion and Conservation, National Research and Innovation Agency
South Tangerang, Indonesia
Email: suli013@brin.go.id

1. INTRODUCTION

Renewable energy sources (RESs) have been proposed to complement conventional energy sources (i.e., fossil fuel) anticipating today's society problem such as global climate change. Various renewable energy is available in the form of, but is not limited to solar energy, wind energy, and hydro energy. Due to the sparse location and decentralized nature of RESs, sometimes it is reasonable to not directly send this energy to a main electrical grid. Instead, the energy will be utilized by a smaller form of electrical grid first to meet the local loads, only the excess or lack of energy of such small electrical grid will be compensated by the main electrical grid. Such a smaller grid is called a 'microgrid' in various literature [1]. It tends to gain higher reliability and more efficient electrical grid systems [2]. DC grid and microgrid can be combined into DC microgrid, which solves the distributed nature of RESs and energy losses due to DC to AC conversion stage [2]–[4]. Moreover, other advantages of DC microgrid have been resumed in [5]. One of them is easier to achieve good power quality than AC microgrid does, thanks to the absence of reactive power problems in DC microgrid [2]. Figure 1 shows an example of DC microgrid structure.

One problem with RESs is that they are intermittent. There is a risk that energy from RESs cannot meet the required demand instantaneously due to intermittency. Different with conventional fossil-based

generation where the fuel is able to be stored, the generated electrical power can be dispatched accordingly. An energy storage system (ESS) is able to be used to store the excess generated energy from RESs then shift the stored energy to be utilized during low RESs energy generation to meet with the demand. In addition, ESSs that are usually assembled also help in stabilizing the DC microgrid.

As already known, the development of electric vehicles (EVs) has grown massively. The article [6] shows that only about 5% of EV battery capacity were utilized for transportation purposes. Hence, the 95% remaining capacity potentially can be employed as an energy buffer for the DC microgrid ecosystems. When the vehicle is parked, the EV battery can assume the role of an ESS from the grid point of view. Moreover, once the batteries have reached their designated lifetime (i.e., underperformed), measures have to be taken to treat them [7], [8]. Disposing of many decommissioned EV batteries is no simple task. If not handled correctly, it will cause devastating effects on the environment. There are two ways to treat these underperformed batteries: recycling and reusing. Instead of completely throwing away these underperformed batteries, one can give these batteries a second life as an ESS in a DC microgrid. These two potential energy storages will give a significant contribution to stabilize the local grid or at least reduce the stationary energy storage size requirement. Indeed, when a lot of EV batteries integrated into the local grid-tied microgrid, this will contribute to the main grid stabilization. For example, some power management methods are capable of utilizing ESSs as virtual inertia in the case of lack of inertia on RES-dominated grid systems.

Khaligh and Dantonio [9] investigated that trends in the propulsion battery voltage level are increasing to meet the increased capacity requirement. Nowadays, components for around 400 V battery voltage levels are well-established and already in the market, while the DC microgrid voltage level fluctuates at about 380-400 V as developed in Indonesia [5]. Battery voltage levels will also fluctuate based on the state of charge of the battery [10]. This voltage fluctuations of two sides in adjacent levels will cause voltage overlap, as discussed in [11]–[13]. Many references [14]–[16] discussed about bi-directional DC-DC converter but do not solve overlapping problems. Khan summarized a brief review of various buck-boost converter topologies suitable to address the overlapping issue for vehicle to grid (V2G) applications. There were two most suitable bidirectional power converter topologies as shown in Figure 2. Based on the type of energy tank, those converters are named as cascaded buck-boost capacitor in the middle (CBB-CIM) [12] as shown in Figure 2(a) and CBB inductor in the middle (CBB-IIM) as shown in Figure 2(b) [17], or simply called in this paper as boost-buck and buck-boost respectively. Then both topologies were compared in detail for some aspects. Overall, boost-buck has better performance than buck-boost, especially in the flexibility to apply an interleaving method. Buck-boost will need full-bridge configuration, while boost-buck just needs half-bridge configuration to apply the interleaving method. Moreover, there will be a circulating current problem in the input loop of buck-boost. Besides that, even though boost-buck has a higher component count, but it has higher overall efficiency than buck-boost has.

On the other side, the main problem of an EV battery is its lifetime. Many factors influence the lifetime of an EV battery. One of these is the switching of the converter gives rise to the current ripple, which can cause capacity to fade and impedance to increase [18]–[20]. Meanwhile, as a power interface, the power converter will be needed if the EV battery is connected to the DC microgrid. The interleaving technique implemented to the converter can solve the current ripple problem [21]–[24].

This paper proposes a power converter to transfer power between EV battery and DC bus of the microgrid. Design procedure considering its functional objectives is described. Since the interleaving method is applied to address the current ripple problem of an EV battery, phase number determination is explained in this paper for the input and output sides of the proposed converter while utilizing the input-output independency of the converter. The switching frequency optimization is also evaluated independently for input and output sides of the converter. Switching frequency is optimized in terms of converter efficiency. With the optimum switching frequency of both sides of the proposed converter, the efficiency of the converter will be maximum since there is a trade-off between switching losses and component losses due to current ripple. The converter efficiency is evaluated based on the switching and conduction losses of each component. Different from Khan in [12], [13] and [25] apart from the converter application, this paper is more focused on the independency of two sides of the converter to gain more flexibility of converter design. Moreover, in this research, the converter parameters will be the same between calculation and experimental to get a matching validation. The parameters are obtained from the datasheets of the converter components in the experiment.

The organization of this paper is the following, section 1 describes recent issues regarding EV battery and DC microgrid, section 2 describes the proposed converter and produces a generalized output-input voltage equation. Section 3 analyses component losses followed by phase number determination. Since switching frequency is optimized in section 4 for converter efficiency, component losses calculation is used for the analysis. As analysis validation, experimental results are presented in section 4. Analysis and experimental results are compared in output-input voltage gain, switching frequency optimization, converter efficiency, and total losses for load change. Finally, a conclusion is made in section 5.
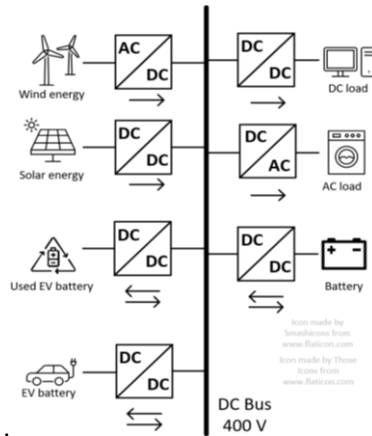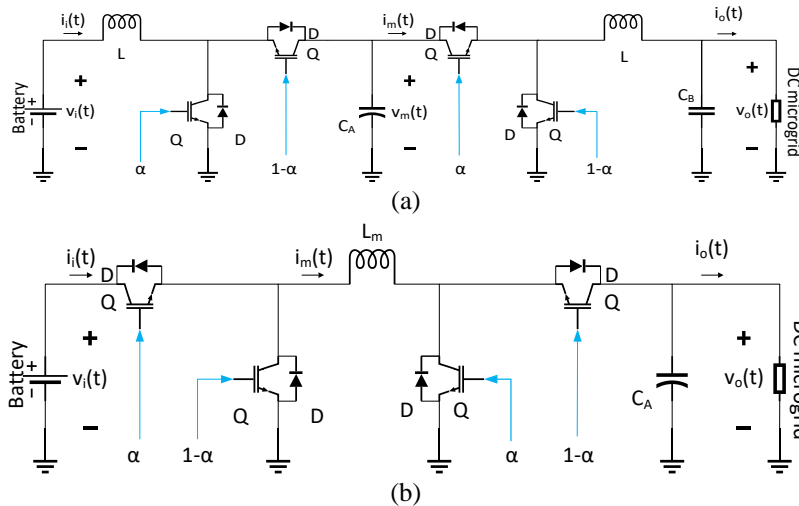
Figure 1. DC microgrid

(a)

(b)

Figure 2. Bidirectional power converters: (a) boost-buck converter and (b) buck-boost converter

2.   BIDIRECTIONAL CASCADED MULTIPHASE BOOST-BUCK CONVERTER

An interfacing converter between EV battery and DC microgrid is needed to transfer energy between them. Some preferable features of the converter are minimum current ripple for the EV batteries [18]–[20], and capable of transferring energy in both directions [12], [17] under EV battery and DC microgrid voltage level fluctuations. EV battery voltage can be higher or lower than DC microgrid bus voltage, or in some literature it can be referred to as overlapping input-output voltages. The converter's efficiency is expected to be over 85% in overall operations. A simple non-isolated converter topology is more preferred for the proposed application in this paper, thus a cascaded-multiphase techniques is implemented into the design of the proposed converter. Figure 3 shows the generalized (unoptimized) proposed converter. The continuous output and input current of this circuit would be another important advantage.

The proposed converter can be deconstructed into two parts: A-part and B-part. A-part has a function to minimize battery current ripple since it is directly connected to the EV battery. The B-part has a function to regulate power flow between EV battery and DC microgrid. The A-part role is realized by implementing multiphase (or in some literature is called as 'interleaved') topology. For battery current ripple minimization, the duty cycle of every leg of A-part is set to be a particular constant-value, which is influenced by the number of A-part phases or legs [21], [22], [24]. Meanwhile, the B-part's duty cycle is allowed to vary depending on the desired power flow (charging or discharging the EV battery) and how fast the battery is charged or discharged.

In Figure 3, the A-part consists of M-phases. Each phase consists of an inductor and a pair of switches in a half-bridge configuration. To achieve a minimum battery current ripple, the value of p/M is taken as a duty cycle for each leg in the A-part. Where M is phase number of A-part converter and p is a positive integer

no more than $M - 1$. The identical switching function of lower switches of each leg in the A-part has a phase angle difference of $(360°)/M$. This means that the A-part has a constant voltage gain. Caution must be taken, so voltage of the middle capacitor $(C_A)\overline{V_m}$ is still in the range of (C_A) capacitor and switches voltage rating.

Referring to Figure 3, the B-part consists of N-phases. The same as the A-part, each phase of the B-part is consisted of an inductor and a pair of switches in a half-bridge configuration but in the opposite direction of their inductor. Taking advantage of the multiphase technique, the on-time of the lower switch of each leg in the B-part is also shifted by $(360°)/N$. The desired power flow rate and direction can be regulated by controlling the current flowing through B-part inductors L_B by changing B-part duty cycle $\overline{D}$.
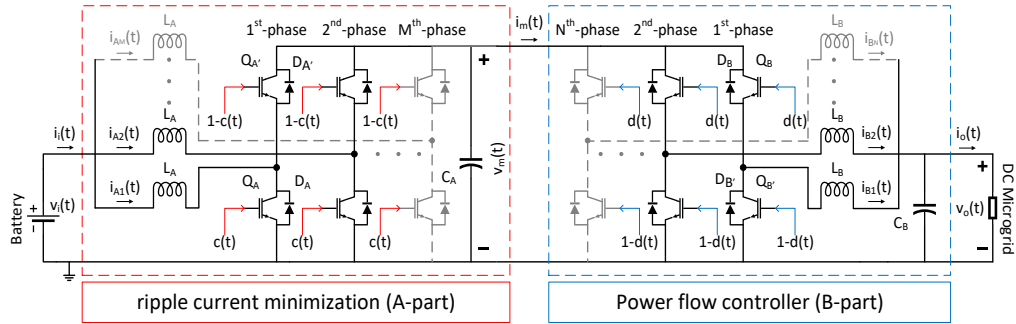

Figure 3. Generalized (unoptimized) proposed bidirectional cascaded multiphase boost-buck converter

By exploiting the independent feature of the cascaded boost-buck converter, the design of the A-part and B-part is carried out separately. In designing the A-part, the objective is to find the number of phases (M) and value of the duty cycle p/M that cause the A-part to meet the EV battery and DC microgrid voltage specification but still retain the feature of battery current ripple minimization. In designing the B-part, the objective is to find the number of phases N that cause the B-part to meet the input-output voltage specification but nothing to do with current ripple minimization of current into DC microgrid. Besides power efficiency and current ripple value, another concern in designing both A-part and B-part is the component specification. Both A-part and B-part must be able to be realized using a common component specification. In short, an optimization to determine the value of M, p, and N of which objective is to obtain an optimum functionality of the proposed converter must be caried out.

Assuming the current flow is the same as shown in Figure 3, A-part and B-part can be regarded as boost and buck converter, respectively. Assuming that the proposed converter is operated in continuous conduction mode (CCM) and all parasitic effects is ignored, the relationship between input (EV battery) and output (DC microgrid) voltage is given in (1).

The effect of parasitic elements omitted in (1) can be included by considering voltage drop in each of switches and inductors. The voltage drop across X (be it insulated gate bipolar transistor or IGBT for Q-indexed or anti-parallel diode for D-indexed) U_X is given by (2).

$$\overline{V}_o = \frac{\overline{D}}{1-\overline{C}}\overline{V}_i \tag{1}$$

$$U_X = V_X + \overline{I}_X R_X \tag{2}$$

Where $\overline{V}_o$, $\overline{V}_i$, $\overline{D}$, $\overline{C}$ are the average steady-state value of output voltage, input voltage, B-part duty cycle as a boost converter, and A-part duty cycle as a buck converter, respectively.

The value of U_X as a function of operating average current $\overline{I}_X$ can be obtained from the output characteristic graph given in the datasheet of the IGBT (including anti-parallel diode output characteristics) by curve fitting. A simple linear regression approximation of U_X gives the parasitic parameters, V_X and R_X, an on-state voltage drop and resistance of the switches, respectively. The state-space averaging of each A-part and B-part in Figure 3 can be done separately. The state-space averaging of A-part when the switch is ON and OFF is given by (3) and (5). Similarly, the state space averaging of B-part when the IGBT is ON and OFF is provided by (4) and (6).

$$\begin{bmatrix} L_A & 0 \\ 0 & C_A \end{bmatrix} \frac{d}{dt} \begin{bmatrix} i_A \\ v_m \end{bmatrix} = \begin{bmatrix} -R_{LA} - R_{QA} & 0 \\ 0 & 0 \end{bmatrix} \begin{bmatrix} i_A \\ v_m \end{bmatrix} + \begin{bmatrix} 0 & 1 & -1 & 0 \\ -1 & 0 & 0 & 0 \end{bmatrix} \begin{bmatrix} i_m \\ v_i \\ V_{QA} \\ V_{DA} \end{bmatrix} \tag{3}$$

$$\begin{bmatrix} L_B & 0 \\ 0 & C_B \end{bmatrix} \frac{d}{dt} \begin{bmatrix} i_B \\ v_o \end{bmatrix} = \begin{bmatrix} -R_{LB} - R_{QB} & -1 \\ N & 0 \end{bmatrix} \begin{bmatrix} i_B \\ v_o \end{bmatrix} + \begin{bmatrix} 0 & 1 & -1 & 0 \\ -1 & 0 & 0 & 0 \end{bmatrix} \begin{bmatrix} i_o \\ v_m \\ V_{QB} \\ V_{DB} \end{bmatrix} \tag{4}$$

$$\begin{bmatrix} L_A & 0 \\ 0 & C_A \end{bmatrix} \frac{d}{dt} \begin{bmatrix} i_A \\ v_m \end{bmatrix} = \begin{bmatrix} -R_{LA} - R_{DA} & -1 \\ M & 0 \end{bmatrix} \begin{bmatrix} i_A \\ v_m \end{bmatrix} + \begin{bmatrix} 0 & 1 & 0 & -1 \\ -1 & 0 & 0 & 0 \end{bmatrix} \begin{bmatrix} i_m \\ v_i \\ V_{QA} \\ V_{DA} \end{bmatrix} \tag{5}$$

$$\begin{bmatrix} L_B & 0 \\ 0 & C_B \end{bmatrix} \frac{d}{dt} \begin{bmatrix} i_B \\ v_o \end{bmatrix} = \begin{bmatrix} -R_{LB} - R_{DB} & 0 \\ N & 0 \end{bmatrix} \begin{bmatrix} i_B \\ v_o \end{bmatrix} + \begin{bmatrix} 0 & 0 & 0 & -1 \\ -1 & 0 & 0 & 0 \end{bmatrix} \begin{bmatrix} i_o \\ v_m \\ V_{QB} \\ V_{DB} \end{bmatrix} \tag{6}$$

Where R_{LA} and R_{LB} are coil resistance of the A-part inductor (L_A) and B-part inductor (L_B), respectively. C_A and C_B are capacitance of A-part and B-part output capacitors, respectively. V_{QA}, R_{QA}, V_{DA}, R_{DA}, V_{QB}, R_{QB}, V_{DB}, R_{DB} are explained in (2), while A-indexed and B-indexed are for A-part and B-part parasitic parameters. $i_A(t)$, $v_m(t)$, $i_B(t)$, $v_o(t)$, $i_m(t)$, $v_i(t)$ and $i_o(t)$ are shown in Figure 3. The (3) and (4) can be turned into (7) by using state-space averaging [26]. The (5) and (6) can also be turned into (8) by using the same method. In (7) and (8) show the average steady-state values of $i_A(t)$, $v_m(t)$, $i_B(t)$ and $v_o(t)$. Both (7) and (8) are obtained by combining (3), (4) and (5), (6) respectively in the steady state.

$$\begin{bmatrix} \overline{I_A} \\ \overline{V_m} \end{bmatrix} = \begin{bmatrix} \frac{1}{M}\left(\frac{1}{1-\bar{c}}\right)\overline{I_m} \\ \frac{\overline{V_i}}{1-\bar{c}} - \left(\frac{\bar{c}}{1-\bar{c}}\right)V_{QA} - V_{DA} - \frac{R_{DA}}{M(1-\bar{c})}\overline{I_m} - \frac{R_{LA}}{M(1-\bar{c})^2}\overline{I_m} - \frac{\bar{c}R_{QA}}{M(1-\bar{c})^2}\overline{I_m} \end{bmatrix} \tag{7}$$

$$\begin{bmatrix} \overline{I_A} \\ \overline{V_m} \end{bmatrix} = \begin{bmatrix} \frac{1}{M}\left(\frac{1}{1-\bar{c}}\right)\overline{I_m} \\ \frac{\overline{V_i}}{1-\bar{c}} - \left(\frac{\bar{c}}{1-\bar{c}}\right)V_{QA} - V_{DA} - \frac{R_{DA}}{M(1-\bar{c})}\overline{I_m} - \frac{R_{LA}}{M(1-\bar{c})^2}\overline{I_m} - \frac{\bar{c}R_{QA}}{M(1-\bar{c})^2}\overline{I_m} \end{bmatrix} \tag{8}$$

Where $\overline{V_i}$, $\overline{I_A}$, $\overline{V_m}$, $\overline{I_B}$, $\overline{V_o}$, $\overline{I_m}$, and $\overline{I_o}$ are the average steady-state value of $v_i(t)$, $i_A(t)$, $v_m(t)$, $i_B(t)$, $v_o(t)$, $i_m(t)$, and $i_o(t)$, respectively.

By substituting $\overline{V_m}$ in (7) into (8), the relationship between $\overline{V_o}$ and $\overline{V_i}$ is given by (9) and is more accurate than (1).

$$\overline{V_o} = \frac{\overline{D}}{1-\bar{c}}\overline{V_i} - \frac{\overline{D}^2 \overline{I_o}}{(1-\bar{c})^2 M}R_{LA} - \frac{\overline{C}\overline{D}}{1-\bar{c}}V_{QA} - \frac{\overline{C}\overline{D}^2 \overline{I_o}}{(1-\bar{c})^2 M}R_{QA} - \overline{D}V_{DA}$$
$$- \frac{\overline{D}^2 \overline{I_o}}{(1-\bar{c})M}R_{DA} - \frac{\overline{I_o}}{N}R_{LB} - \overline{D}V_{QB} - \frac{\overline{D}\overline{I_o}}{N}R_{QB} - (1-\overline{D})V_{DB} - \frac{(1-\overline{D})\overline{I_o}}{N}R_{DB} \tag{9}$$

The output voltage expression of the generalized proposed converter in (9) describes a more realistic equation of the output voltage and it is always lower than the ideal output voltage in (1). If all parasitic components are ignored, or considered to be inexistent, then (9) turns back into (1), which is the ideal output voltage.

3. LOSSES ANALYSIS OF THE PROPOSED CONVERTER
3.1. Current analysis

Parasitic elements existing in each converter components cause power losses. By calculating power losses in each component, power losses of the proposed converter can be obtained [27]. Currents through the inductor need to be defined to calculate power losses. The converter is assumed to be operated in CCM and the inductor is not saturated. The RMS inductor current can be defined in (10) constituted by average current ($\overline{I_L}$) and RMS value of current ripple $\left(\sqrt{\frac{\Delta i_L^2}{12}}\right)$. The inductor current ripple (Δi_L) is defined by (11).

$$i_{L,rms} = \sqrt{\left(\overline{I_L}^2 + \frac{\Delta i_L^2}{12}\right)} \tag{10}$$

$$\Delta i_L = \left(\frac{\overline{V_L}}{L}\right)(t_{ON}) \tag{11}$$

t_{ON} is the time during which voltage $\overline{V_L}$ is applied to the inductor. For the case of the generalized proposed converter in Figure 3, (10) becomes (12) and (14), and (11) becomes (13) and (15).

$$i_{A,rms} = \sqrt{\left(\overline{I_A}^2 + \frac{\Delta i_A^2}{12}\right)} \tag{12}$$

$$\Delta i_A = \left(\frac{\overline{V_l}}{L_A}\right)\left(\frac{\bar{C}}{f_A}\right) \tag{13}$$

$$i_{B,rms} = \sqrt{\left(\overline{I_B}^2 + \frac{\Delta i_B^2}{12}\right)} \tag{14}$$

$$\Delta i_B = \left(\frac{\overline{V_m} - \overline{V_o}}{L_B}\right)\left(\frac{\overline{D}}{f_B}\right) \tag{15}$$

Where, $i_{A,rms}$, $i_{B,rms}$, $\overline{I_A}$, $\overline{I_B}$, Δi_A, Δi_B, f_A, and f_B are A-part and B-part rms value of inductor current, A-part and B-part average value of inductor current, A-part and B-part inductor peak-to-peak current ripple, A-part and B-part switching frequency, respectively. The relationship between averaged inductor current and input-output voltage are $\overline{I_A} = \frac{\overline{I_l}}{M}$ and $\overline{I_B} = \frac{\overline{I_o}}{N}$. The relationship between output and input current is assumed to be $\overline{I_o} = \left(\frac{1-\bar{C}}{\overline{D}}\right)\overline{I_l}$.

3.2. Inductor copper losses

Besides coil DC resistance, current ripple flowing in each inductor also generates conduction losses due to skin-effect. Therefore, there is a resistance of AC. In this research, the AC resistance was measured at 10 kHz, which is the desired value of the switching frequency operation. Inductor copper losses in the inductor L_A (P_{LA}) and L_B (P_{LB}) are given by (16) and (17).

$$P_{LA} = M\left(\overline{I_A}^2 R_{LA,DC} + \frac{\Delta i_A^2}{12} R_{LA,AC}\right) \tag{16}$$

$$P_{LB} = N\left(\overline{I_B}^2 R_{LB,DC} + \frac{\Delta i_B^2}{12} R_{LB,AC}\right) \tag{17}$$

Where, $R_{LA,DC}$, $R_{LA,AC}$, $R_{LB,DC}$, and $R_{LB,AC}$ are DC resistance and AC resistance of A-part and B-part inductor respectively. The DC resistance value depends on the length of the wire used, or the number of turns of the inductor, so it relates to the inductance of the inductor. The larger the inductance, the larger the DC resistance, and the higher the conduction losses produced. Conduction losses due to AC resistance is affected by the square rms value of the current ripple flowing through the inductor. The larger the current ripple generated, the larger the conduction losses due to AC resistance. The AC resistance can be reduced by using Litz-wire instead of single conductors.

3.3. Core losses

Inductor core losses (P_{CA} and P_{CB}) can be calculated from peak-to-peak magnetic flux density ΔB in gauss (18) and operating switching frequency (f_A and f_B). Where, L_A, N_A, and A_A are inductance in Henries, number of turns, cross-sectional area (cm^2) of A-part inductor, respectively. The empirical-based expression of core losses in mW/cm^3 is shown in (19) obtained from the datasheet of the inductor core used. Where, f_A is A-part switching frequency in kHz.

$$\Delta B_A \approx \frac{L_A \Delta i_A \times 10^8}{N_A A_A} \tag{18}$$

$$P_{CA} = \left(\frac{\Delta B_A}{2000}\right)^{2.225}\left(4.584 f_A + 0.0238 f_A^{1.966}\right)M \tag{19}$$

Thus, a higher peak to peak flux density and switching frequency will yield higher inductor core losses. From (18), inductor core losses are able to be reduced by reducing inductance or current ripple, or by increasing the number of turns or cross-sectional area of inductor core. In (18) and (19) are also applicable for B-part inductor core losses calculation.

3.4. Switch losses
3.4.1. IGBT losses

In this research, IGBTs are used as power switches. Due to parasitic elements present in IGBT, as shown in (2), conduction losses also occur in IGBT. Average conduction losses in each A-part (P_{QA}) and B-part (P_{QB}) IGBT are given by (20) and (21).

$$P_{QA} = \left(R_{QA}\bar{C}\left(\bar{I_A}^2 + \frac{\Delta i_A{}^2}{12} \right) + V_{QA}\overline{I_{QA}} \right) M \tag{20}$$

$$P_{QB} = \left(R_{QB}\bar{D}\left(\bar{I_B}^2 + \frac{\Delta i_B{}^2}{12} \right) + V_{QB}\overline{I_{QB}} \right) N \tag{21}$$

Derivation of the equations is well described in [28]. Where, $\overline{I_{QA}} = \bar{C}\bar{I_A}$ and $\overline{I_{QB}} = \bar{D}\bar{I_B}$. On state voltage drop of the IGBT (V_Q) multiplied by average current flowing ($\bar{I_Q}$) becomes part of the converter losses. As well as on state resistance (R_Q) multiplied by the square of the rms value of current flowing (i_{rms}). Then the resistive losses are quadratically increasing to the increase in load current.

3.4.2. Anti-parallel diode losses

In general, a fast recovery anti-parallel diode is integrated into each IGBT. The average conduction losses in anti-parallel diode (P_{DA} and P_{DB}) can be calculated similarly as in IGBT. The equations are given by (22) and (23).

$$P_{DA} = \left(R_{DA}(1 - \bar{C})\left(\bar{I_A}^2 + \frac{\Delta i_A{}^2}{12} \right) + V_{DA}\overline{I_{DA}} \right) M \tag{22}$$

$$P_{DB} = \left(R_{DB}(1 - \bar{D})\left(\bar{I_B}^2 + \frac{\Delta i_B{}^2}{12} \right) + V_{DB}\overline{I_{DB}} \right) N \tag{23}$$

Where, $\overline{I_{DA}} = (1 - \bar{C})\bar{I_A}$ and $\overline{I_{DB}} = (1 - \bar{D})\bar{I_B}$, the same with IGBT losses analysis, there is also quadratic resistive losses part produced by conducting diode.

3.4.3. Switching losses

Switching losses of the IGBT (P_{SA} and P_{SB}) and diode reverse recovery as a function of operating average-current can be obtained by curve fitting of switching energy loss graph given in the corresponding IGBT datasheet. The losses show the wasted energy when the IGBT is turned on or off and diode is turned off. Losses due to switching of IGBT are given by (24) and (25).

$$P_{SA} = \left(E_{ON,A}[i_{QA,rms}] + E_{OFF,A}[i_{QA,rms}] + E_{RR,A}[i_{QA,rms}] \right)f_A M \tag{24}$$

$$P_{SB} = \left(E_{ON,B}[i_{QB,rms}] + E_{OFF,B}[i_{QB,rms}] + E_{RR,B}[i_{QB,rms}] \right)f_B N \tag{25}$$

Where, E_{ON}, E_{OFF}, and E_{RR} are energy dissipated as a function of rms current flowing when the switch turned-on, turned-off, and the diode turned-off respectively. In general, the higher the switching frequency is, the higher the switching losses will be.

3.5. Phase number determination of the proposed converter

The phase number determination of the proposed converter is tied to the desired voltage specification of the converter and its input-output objects. To demonstrate the determination process, the specification of the EV battery is based on Tesla model S as in (https://www.evspecifications.com/en/model/89e4a4, accessed on Oct. 07, 2021). The operating voltage range of the EV battery is from 240 V to 400 V. The nominal DC microgrid voltage is 400 V and able to fluctuate from 350 V to 450 V [2]. The minimum power passing the converter is assumed to be 1440 W. This will be the criteria to choose the minimum inductance value to ensure that the converter will operate in CCM that is described in fourth part. The maximum power passing the converter is assumed to be 9600 W which is used to calculate the current rating of switches and inductors in fourth part. Table 1 shows all parameters needed to do the determination process.

A particular constant-value is assigned as the duty cycle of the A-part switches. The relationship between constant duty cycle and the number of legs that give minimum current ripple has been discussed earlier in the previous section. The possible arrangements of the number of legs and duty cycle of A-part that cause

minimum battery current ripple are shown in Table 2. For simplification, idealized boost converter voltage ratio (26) is used to plot the value of $\overline{V_m}$ as a function of battery voltage $\overline{V_l}$ variations that is shown in Figure 4.

$$\overline{V_m} = \frac{1}{1-\bar{C}}\overline{V_l}$$ (26)

Table 1. Specification for converter optimization

Parameter		Value
Battery voltage ($\overline{V_l}$)		240 – 400 V
Middle capacitor voltage ($\overline{V_m}$)		450 – 600 V
DC microgrid voltage ($\overline{V_o}$)		350 – 450 V
Power	Maximum	9625 W
	Minimum	1440 W
Minimum efficiency		85%
Battery current	Maximum	40.1 A
	Minimum	3.6 A
Current supplied to the DC microgrid	Maximum	27.5 A
	Minimum	3.2 A

Table 2. Possible arrangement for a-part for converter optimization

Arrangement No.	Number of A-part legs	Duty cycle
I	2	0.5
II	3	0.333
III	3	0.666
IV	4	0.25
V	4	0.5
VI	4	0.75

There are several borders in Figure 4. Horizontal dashed line borders indicate maximum allowed and minimum required value for the middle capacitor (C_A) voltage $\overline{V_m}$. The maximum value of $\overline{V_m}$ is decided based on the availability of capacitors and switches in the market. In this paper, it is preferred that every component to be loaded half of its maximum voltage rating. Since 1200 V capacitor is easily found in the market, the maximum allowed value of $\overline{V_m}$ is set to be 600 V. The minimum required value of $\overline{V_m}$ is determined from maximum DC microgrid voltage at 450 V. $\overline{V_m}$ have to be higher than the maximum DC microgrid voltage $\overline{V_o}$ even when the battery is at its lowest voltage level to make sure the bidirectional power transfer to happen. Vertical dashed line borders indicate maximum and minimum value for EV battery voltage $\overline{V_l}$ range as described in Table 1.
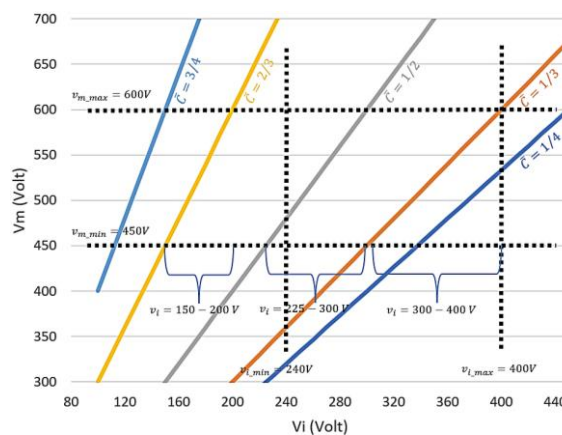

Figure 4. The middle capacitor (C_A) voltage $\overline{V_m}$ as a function of battery voltage $\overline{V_l}$ variations

Shown in Figure 4 and Table 2, phase number optimization can be concluded. For $\overline{V_l}$ range from 300 to 400 V, A-part duty cycle needs to be $\bar{C} = 1/3$ so that $\overline{V_m}$ is in the range from 450 to 600 V. Arrangement II is chosen in this $\overline{V_l}$ range. Arrangement IV is not chosen because one more leg will be needed and $\overline{V_l}$ range is

narrower than $\overline{V_i}$ range with arrangement II. For $\overline{V_i}$ range from 240 to 300 V, A-part duty cycle needs to be $\bar{C} = 1/2$ so that $\overline{V_m}$ in the range from 450 to 600 V. Actually, arrangement I or V will be needed but arrangement II can still be used by disabling one of three legs and becomes arrangement I. Moreover, arrangement II can be utilized for lower voltage of $\overline{V_i}$ from 150 to 200 V by setting $2/3$ as A-part duty cycle $\bar{C}$. One phase is sufficient for the B-part since its role is just to control the power flow direction of the proposed converter and has nothing to do with current ripple minimization. Then the proposed converter with phase number optimization is shown in Figure 5.
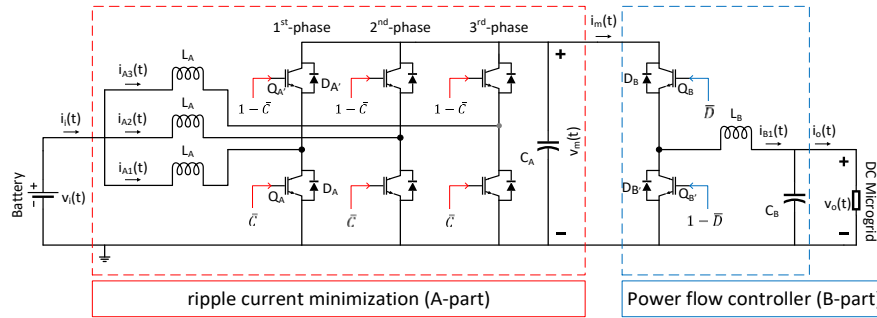

Figure 5. The proposed converter with phase number optimization

4. EXPERIMENTAL RESULTS AND DISCUSSIONS

The performance of the proposed converter was examined unidirectionally. A three-phase autotransformer and a rectifier with a capacitor filter were used as DC power supply for the converter. Some variable wire-wound resistors were installed in parallel as a DC load. Power was measured on both sides of the proposed converter using a power meter, as shown in Figure 6. A bidirectional power flow control is not shown in this paper, but it is discussed in another experimental research paper of detailed control method [29]. The power flow control can be done by varying the duty cycle of B-part (microgrid side) switches.
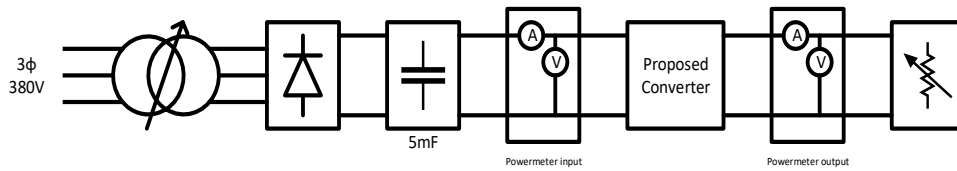

Figure 6. Experimental setup block diagram

4.1. Converter specification

Referring to Figure 5, a downscaled prototype of the proposed converter has been manufactured. The components used in this prototype determine its maximum working conditions. As an energy buffer, the middle capacitor C_A is chosen to have large capacitance to minimize the voltage ripple of v_m. The large value of C_A capacitance makes the separation between A-part and B-part more valid, so the A-part and B-part can be regarded as independent. Four paralleled electrolyte capacitors, each rated at 47 µF, and four paralleled 220 nF film capacitor MKP or metallized polypropylene film capacitors types are used as middle capacitors C_A. The capacitor voltage is rated at 450 V. Sendust type of toroid material with the series of KS200-060A is used as inductor core. By rough calculation, with the core mentioned, all inductors are capable of conducting an average-currents around 7 A for A-part and 21 A for B-part without being saturated.

IGBT FGH40N60UFD with voltage rating and nominal current of 600 V and 40 A are used as switches of A-part of the proposed converter, while KGF50N60KDA with a rating of 600 V and 50 A are used for B-part. B-part switches have a higher current rating than A-part switches have because B-part has fewer phase numbers causing each switch in B-part to carry a higher current than each switch in A-part does. All IGBTs can accommodate maximum operating current of all inductors easily without overloading and can withstand the maximum operation voltage of C_A, which is 225 V. Each chosen IGBT has been featured with a fast recovery anti-parallel diode. All parasitic values and characteristics of IGBTs and their anti-parallel diode can be found in their datasheet.

Table 3. Specification for scaled-down prototype

Parameter		Value
Battery voltage (v_i)		80 – 133 V
Middle capacitor voltage (v_m)		150 – 200 V
DC microgrid voltage (v_o)		116 – 150 V
Power	Maximum	1605 W
	Minimum	240 W
Minimum efficiency		85%
Battery current	Maximum	20.1 A
	Minimum	1.8 A
Current supplied to the DC microgrid	Maximum	13.8 A
	Minimum	1.6 A

For the limitation of middle capacitor voltage rating and inductor current rating, the specification of the proposed converter shown in Table 3 is scaled down from the actual specification shown in Table 1. From the phase number optimization process shown in Table 2 and Figure 4, the working duty cycle of the scaled battery voltage range, 80-100 V and 100-135 V are 0.5 and 0.333, respectively. Then the C_A maximum voltage is 202.5 V ($135 \times \frac{1}{1-0.333}$).

Since the proposed converter is intended for bidirectional energy transfer, all inductors are designed so the proposed converter can still operate in CCM on low currents. The critical condition between CCM and discontinuous conduction mode (DCM) operations happens when the value of minimum inductor current I_{min} is zero ampere. Then the critical condition of inductor conduction generally can be determined by critical inductance (L_{crit}) in (27) for the DC-DC boost converter. When I_{min} is 0 A, the input average-current of DC-DC boost converter (I_{avg}) is $I_{max}/2$. Each inductor is designed so that the proposed converter can work in a worst-case scenario from Table 3. When the proposed converter operates in battery average-current as low as 1.8 A, each inductor will be conducting an average-current of 0.6 A. Minimum scaled version of battery voltage is 80V when A-part duty cycle is at 0.5. All IGBTs are assumed to be operated at 10 kHz. Therefore, the critical inductance of the A-part inductor calculated with (27) is 3.33 mH. (27) also applicable for B-part inductor calculation by assuming DC microgrid voltage as input $\overline{V_I}$. The worst-case of B-part is when $\overline{V_I}$ is minimum at 116 V and $\overline{C}$ is maximum at 0.5. Then the critical inductance for the B-part inductor is 1.82 mH.

$$L_{crit} = \frac{\overline{C V_I}}{2 \overline{I_{avg}} f_{sw}} \tag{27}$$

Parameters of customized hand-made inductors were measured using Sanwa LCR700 at a frequency of 10 kHz. The inductance and DC and AC series resistance of each A-part inductor is around 4.225 mH, 0.44 Ohm, and 0.845 Ohm, while for B-part inductor is 2.099 mH, 0.22 Ohm, and 0.462 Ohm.

4.2. Battery current ripple
The input current, together with each of the A-part inductor currents shown in Figure7, was captured using oscilloscope through LEM current transducers. To capture a triangle-wave of the inductor current, a low-pass noise filter was not used. Consequently, there are a lot of spikes captured, as in Figure 7. There is almost identical current ripple in each A-part inductor that phase shifted almost evenly so that theoretically these current ripples will cancel each other. Battery current ripple minimization by multiphase technique is confirmed by the absence of currents ripple due to IGBT switching in the battery currents. Minimum current ripple at A-part input is achieved when the duty cycle of this part of the converter is kept constant at a value of either $1/3$ or $2/3$.

Figure 7. Battery current and a-part inductor current waveforms

4.3. Output-input voltage gain

Load resistance and duty cycle of B-part switches were set to obtain output current of 2 A and 8 A. Experimental and calculation of voltage ratio in terms of B-part duty cycle ($\bar{D}$) variations and constant output current at 2 A and 8 A are shown in Figure 8. It shows that the analytical calculation of voltage gain is validated by experimental results with some tolerated differences. The input (representing a battery) voltage was set to 130V and 60 V when $\bar{C} = 1/3$ in Figure 8(a) and $\bar{C} = 2/3$ in Figure 8(b), respectively. This distinction is required to keep the CA voltage under its maximum designated value of 225 V. This part of the experiment showed that the proposed converter could accommodate a lower battery voltage by only changing the A-part duty cycle $\bar{C}$ to be 2/3. The wide input range made the proposed converter suitable for various voltage ranges of ESSs. Besides that, the main feature of the proposed converter, bidirectionally buck-boost operation, is also shown in Figure 8. When the voltage gain is less than unity, the proposed converter works as a buck converter. Reciprocally when the voltage gain is more than unity, the proposed converter works as a boost converter.

4.4. Switching frequency optimization

By analytical calculation in third part, switching losses on IGBT will be increasing as switching frequency is increased, as shown in (24) and (25). However, current ripple due to IGBT switching will be decreasing due to the lesser conduction time of the IGBT to charge the inductors, as shown in (12)-(15). Current ripple contributes to the power losses of each component, as analysed in third part. Therefore, there is a trade-off in the determination of switching frequency to the converter efficiency.

By this part of the experiment, the switching frequency was varied to see its influence on the proposed converter efficiency. The experiment was done by keeping one part of the proposed converter at a constant frequency while the switching frequency of the other part was varied. The output current was also varied by varying load resistance. Figure 9 shows that experimental results have validated the calculation results of the proposed converter efficiency for switching frequency variation. Figure 9(a) shows the results of the proposed converter efficiency when the B-part switching frequency (f_B) was kept constant, and Figure 9(b) when the A-part switching frequency (f_A) was kept constant. Both Figure 9(a) and Figure 9(b) show experimental and calculation results of converter efficiency at different output current (5 A and 8 A). As a result, the converter has an optimum efficiency when f_A nor f_B are around 10 kHz.
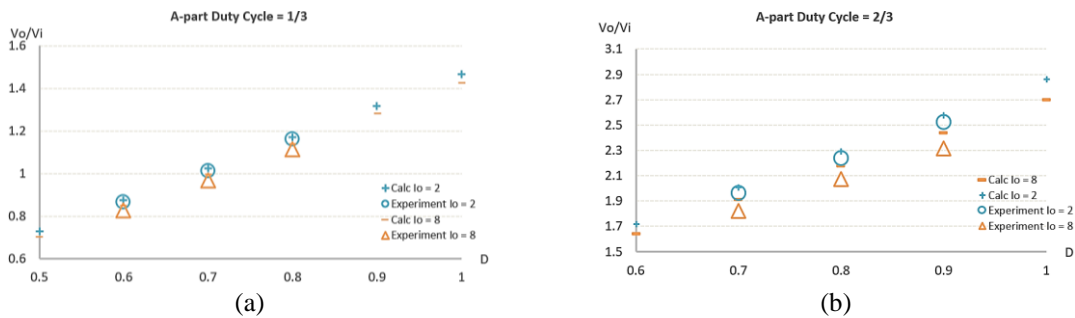

Figure 8. Calculation and experimental result of output-input voltage ratio at (a) $\bar{C} = 1/3$ and (b) $\bar{C} = 2/3$
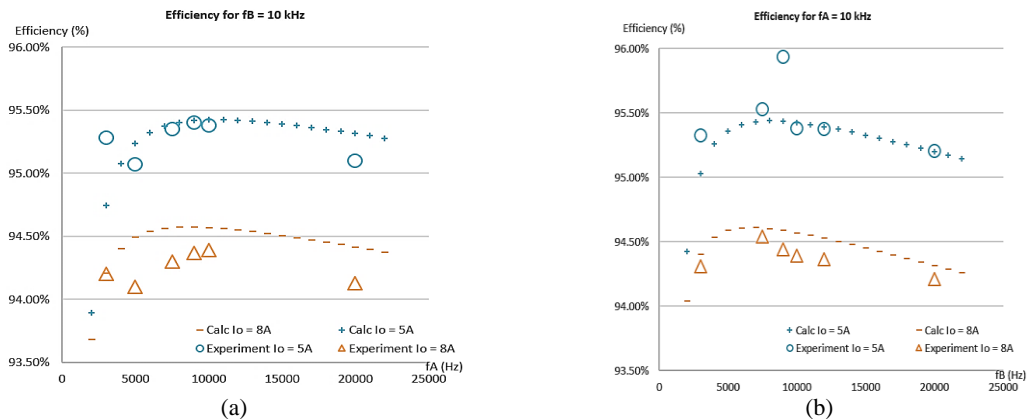

Figure 9. Calculation and experimental results of efficiency for Io 5 A and 8 A (a) in terms of f_A variation with fixed f_B at 10 kHz and (b) in terms of f_B variation with fixed f_A at 10 kHz

4.5. Converter efficiency

The comparison of calculation and experimental efficiency of the proposed converter to different load power levels is shown in Figure 10. The value of $\bar{C}$ and $\bar{D}$ were also varied. It shows that efficiency analysis has been validated with the experimental results since they are in a similar trend. As the power increment, the converter experienced a deeper efficiency drop when the value of $\bar{C}$ was 2/3 in Figure 10(a) than when it was 1/3 in Figure 10(b). This is due to the increase in current flow for a higher value of $\bar{C}$ following the efficiency analysis in third part that the losses from all components are directly proportional to the working current. Even for resistive parasitic components, the increase in losses is quadratic.

4.6. Converter total losses

Instead of efficiency, the experimental results can also be represented in Figure 11 in terms of total losses, where in Figure 11(a) for A-part duty cycle 2/3 and in Figure 11(b) for A-part duty cycle 1/3. The comparison in Figure 11 shows that experimental results validate the component losses analysis in third part. Therefore, power losses contributed by each parasitic component with different load power levels can be represented as in Figure 12. From Figure 12(a), the series resistance losses (PL) of the inductor increase quadratically with the increase in load, but for losses from other parasitic components, the quadratic character is not visible. This is caused by the relatively high series resistance of the inductor, while the IGBT and diode resistance is relatively small. It would be different if the switch used were a silicon MOSFET where the drain-source resistance is usually higher than the IGBT has. As shown in Figure 12(b), starting from the input power of about 420 watts, the portion of losses from the series resistance of the inductor are 25% and quadratically increasing to 48% when the input power is 1200 watts. For that reason, the efficiency can be increased significantly by decreasing the series resistance of the inductor. This can be achieved by increasing the cross-sectional area of the inductor wire or reducing the inductance. Increased efficiency can also be obtained by using new material types of switches such as SiC and GaN-based switches. The portion of core losses has a low contribution on total converter losses. It shows a margin to optimize total inductor losses that have a trade-off between core losses and inductor conduction losses. This will be conducted in the next investigation.
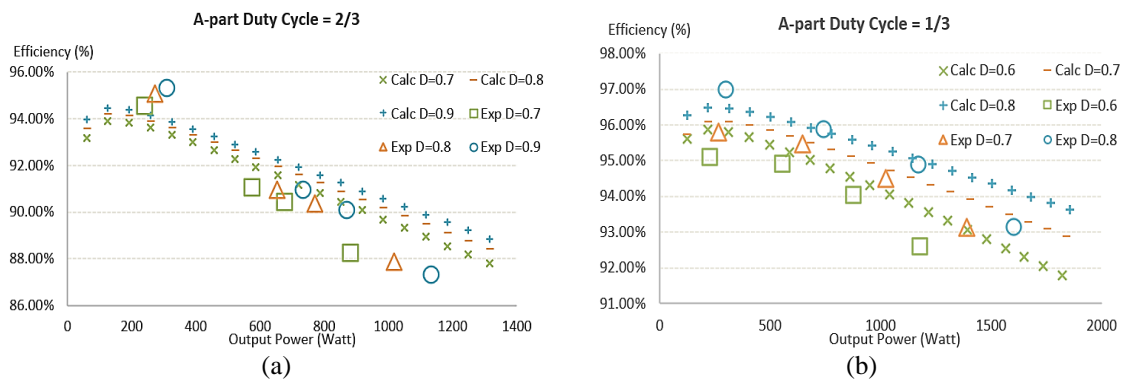

Figure 10. Efficiency on power load change for some value of $\bar{D}$ with (a) $\bar{C} = 1/3$ and (b) $\bar{C} = 2/3$
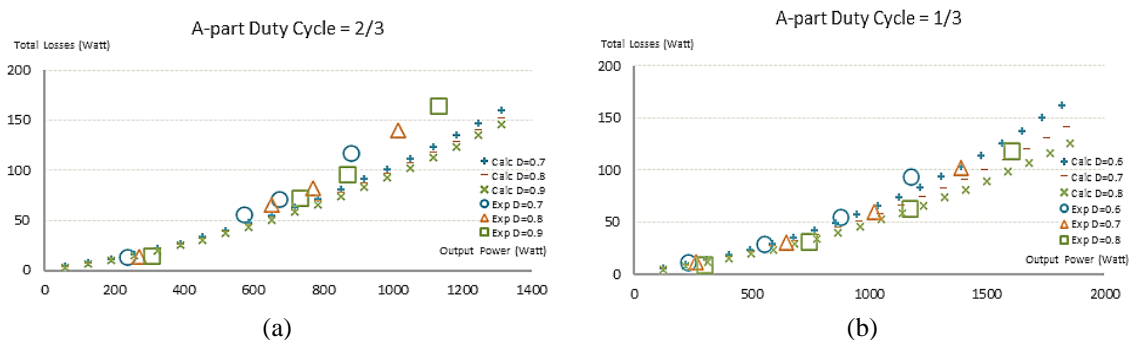

Figure 11. Total losses on power load change for some value of $\bar{D}$ with (a) $\bar{C} = 1/3$ and (b) $\bar{C} = 2/3$
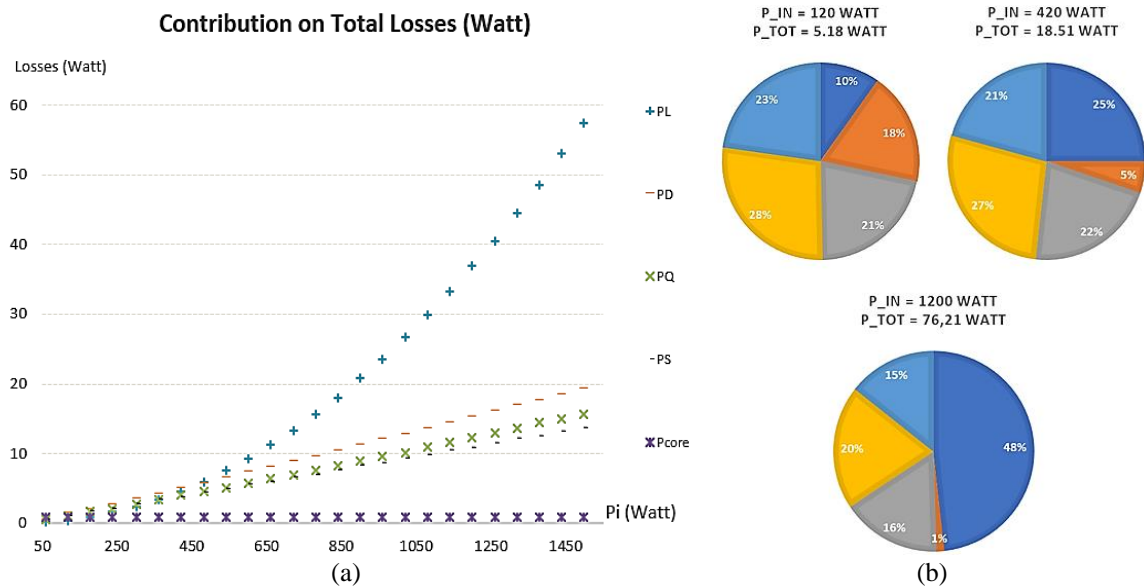
Figure 12. Contribution on total losses in terms of power load change (a) in % and (b) in watt

5. CONCLUSION

An optimized cascaded multiphase bidirectional boost-buck converter has been proposed. A scaled-down prototype has verified battery current ripple minimization and output-input overlapping voltage operation. In the power range between 60 W to 1850 W, the minimum efficiency is 91.7% for $\bar{C} = 1/3$ and 87.31% for $\bar{C} = 2/3$ and the maximum is 96.97% can be achieved. Overall, the experimental results have validated the analytical calculation given in this paper. The proposed converter is well suited to the bidirectional application for EV battery interface. A bidirectional power flow control can be done by varying the duty cycle of B-part (microgrid side) switches discussed in another experimental research paper of detailed control method. Efficiency improvement of the proposed converter by component parameter optimization, especially by inductance reduction or even operated in discontinuous conduction mode (DCM), will be covered in the next investigation.

REFERENCES

[1] G. V. B. Kumar, K. Palanisamy, P. Sanjeevikumar, and S. M. Muyeen, "Analysis of control strategies for smoothing of solar PV fluctuations with storage devices," *Energy Reports*, vol. 9, pp. 163–177, 2023, doi: 10.1016/j.egyr.2022.11.176.
[2] D. Kumar, F. Zare, and A. Ghosh, "DC Microgrid Technology: System Architectures, AC Grid Interfaces, Grounding Schemes, Power Quality, Communication Networks, Applications, and Standardizations Aspects," *IEEE Access*, vol. 5, no. c, pp. 12230–12256, 2017, doi: 10.1109/ACCESS.2017.2705914.
[3] T. Dragicevic, X. Lu, J. C. Vasquez, and J. M. Guerrero, "DC Microgrids - Part I: A Review of Control Strategies and Stabilization Techniques," *IEEE Transactions on Power Electronics*, vol. 31, no. 7, pp. 4876–4891, 2016, doi: 10.1109/TPEL.2015.2478859.
[4] T. Dragičević, X. Lu, J. C. Vasquez, and J. M. Guerrero, "DC Microgrids - Part II: A Review of Power Architectures, Applications, and Standardization Issues," *IEEE Transactions on Power Electronics*, vol. 31, no. 5, pp. 3528–3549, 2016, doi: 10.1109/TPEL.2015.2464277.
[5] T. Ardriani *et al.*, "A dc microgrid system for powering remote areas," *Energies*, vol. 14, no. 2, 2021, doi: 10.3390/en14020493.
[6] A. Sharma and S. Sharma, "Review of power electronics in vehicle-to-grid systems," *Journal of Energy Storage*, vol. 21, no. November 2018, pp. 337–361, 2019, doi: 10.1016/j.est.2018.11.022.
[7] M. H. S. M. Haram, J. W. Lee, G. Ramasamy, E. E. Ngu, S. P. Thiagarajah, and Y. H. Lee, "Feasibility of utilising second life EV batteries: Applications, lifespan, economics, environmental impact, assessment, and challenges," *Alexandria Engineering Journal*, vol. 60, no. 5, pp. 4517–4536, 2021, doi: 10.1016/j.aej.2021.03.021.
[8] E. Martinez-Laserna *et al.*, "Battery second life: Hype, hope or reality? A critical review of the state of the art," *Renewable and Sustainable Energy Reviews*, vol. 93, no. April, pp. 701–718, Oct. 2018, doi: 10.1016/j.rser.2018.04.035.
[9] A. Khaligh and M. Dantonio, "Global Trends in High-Power On-Board Chargers for Electric Vehicles," *IEEE Transactions on*

Vehicular Technology, vol. 68, no. 4, pp. 3306–3324, 2019, doi: 10.1109/TVT.2019.2897050.

[10] P. S. Tomar, A. K. Sharma, and K. Hada, "Energy storage in DC microgrid system using non-isolated bidirectional soft-switching DC/DC converter," in *2017 6th International Conference on Computer Applications In Electrical Engineering-Recent Advances (CERA)*, Oct. 2017, vol. 2018-Janua, pp. 439–444. doi: 10.1109/CERA.2017.8343370.

[11] Y. Du, X. Zhou, S. Bai, S. Lukic, and A. Huang, "Review of non-isolated bi-directional DC-DC converters for plug-in hybrid electric vehicle charge station application at municipal parking decks," in *Conference Proceedings - IEEE Applied Power Electronics Conference and Exposition - APEC*, 2010, no. 1, pp. 1145–1151. doi: 10.1109/APEC.2010.5433359.

[12] M. A. Khan, I. Husain, and Y. Sozer, "A Bidirectional DC–DC Converter With Overlapping Input and Output Voltage Ranges and Vehicle to Grid Energy Transfer Capability," *IEEE Journal of Emerging and Selected Topics in Power Electronics*, vol. 2, no. 3, pp. 507–516, 2014, doi: 10.1109/jestpe.2014.2305157.

[13] M. A. Khan, A. Ahmed, I. Husain, Y. Sozer, and M. Badawy, "Performance Analysis of Bidirectional DC-DC Converters for Electric Vehicles," *IEEE Transactions on Industry Applications*, vol. 51, no. 4, pp. 3442–3452, 2015, doi: 10.1109/TIA.2015.2388862.

[14] B. Benlahbib *et al.*, "An experimental investigation design of a bidirectional DC-DC buck-boost converter for PV battery charger system," *International Journal of Power Electronics and Drive Systems (IJPEDS)*, vol. 14, no. 4, p. 2362, Dec. 2023, doi: 10.11591/ijpeds.v14.i4.pp2362-2371.

[15] R. Moualek, N. Benamrouche, N. Benyahia, and A. Bousbaine, "Hybrid multi power sources PEMFC/battery/supercapacitor real time setup energy conversion system," *International Journal of Power Electronics and Drive Systems*, vol. 14, no. 3, pp. 1844–1854, 2023, doi: 10.11591/ijpeds.v14.i3.pp1844-1854.

[16] S. Neelagiri and P. Usha, "Modelling and control of grid connected microgrid with hybrid energy storage system," *International Journal of Power Electronics and Drive Systems (IJPEDS)*, vol. 14, no. 3, p. 1791, 2023, doi: 10.11591/ijpeds.v14.i3.pp1791-1801.

[17] S. Waffler and J. W. Kolar, "A Novel Low-Loss Modulation Strategy for High-Power Bidirectional Buck + Boost Converters," *IEEE Transactions on Power Electronics*, vol. 24, no. 6, pp. 1589–1599, 2009, doi: 10.1109/TPEL.2009.2015881.

[18] M. Broussely *et al.*, "Main aging mechanisms in Li ion batteries," *Journal of Power Sources*, vol. 146, no. 1–2, pp. 90–96, 2005, doi: 10.1016/j.jpowsour.2005.03.172.

[19] K. Uddin, A. D. Moore, A. Barai, and J. Marco, "The effects of high frequency current ripple on electric vehicle battery performance," *Applied Energy*, vol. 178, pp. 142–154, 2016, doi: 10.1016/j.apenergy.2016.06.033.

[20] W. Waag, S. Käbitz, and D. U. Sauer, "Experimental investigation of the lithium-ion battery impedance characteristic at various conditions and aging states and its influence on the application," *Applied Energy*, vol. 102, pp. 885–897, 2013, doi: 10.1016/j.apenergy.2012.09.030.

[21] P. A. Dahono, S. Riyadi, A. Mudawari, and Y. Haroen, "Output ripple analysis of multiphase dc-dc converters," in *Proceedings of the International Conference on Power Electronics and Drive Systems*, 1999, vol. 2, pp. 626–631. doi: 10.1109/peds.1999.792732.

[22] L. K. M. Pereira, S. I. Seleme, and J. L. da Silva, "Generalized Mathematical Model for an N-cell Interleaved Boost Converter," in *2019 IEEE 15th Brazilian Power Electronics Conference and 5th IEEE Southern Power Electronics Conference (COBEP/SPEC)*, Dec. 2019, pp. 1–6. doi: 10.1109/COBEP/SPEC44138.2019.9065683.

[23] H.-B. Shin, J.-G. Park, S.-D. Chang, and H.-C. Choi, "Generalized analysis of multi-phase interleaved boost converter," *International Journal of Electronics*, vol. 92, no. 1, pp. 1–20, Jan. 2005, doi: 10.1080/00207210412331332943.

[24] H.-B. Shin, J.-G. Park, S.-K. Chung, H.-W. Lee, and T. A. Lipo, "Generalised steady-state analysis of multiphase interleaved boost converter with coupled inductors," *IEE Proceedings - Electric Power Applications*, vol. 152, no. 3, p. 584, 2005, doi: 10.1049/ip-epa:20045052.

[25] D. W. Spier, G. G. Oggier, and S. A. O. da Silva, "Dynamic modeling and analysis of the bidirectional DC-DC boost-buck converter for renewable energy applications," *Sustainable Energy Technologies and Assessments*, vol. 34, no. May, pp. 133–145, 2019, doi: 10.1016/j.seta.2019.05.002.

[26] R. D. Middlebrook and S. Cuk, "A general unified approach to modelling switching-converter power stages," in *1976 IEEE Power Electronics Specialists Conference*, Jun. 2015, vol. 21, no. 1, pp. 18–34. doi: 10.1109/pesc.1976.7072895.

[27] C. Wang, R. Xiong, H. He, X. Ding, and W. Shen, "Efficiency analysis of a bidirectional DC/DC converter in a hybrid energy storage system for plug-in hybrid electric vehicles," *Applied Energy*, vol. 183, pp. 612–622, 2016, doi: 10.1016/j.apenergy.2016.08.178.

[28] H. Hafezi and R. Faranda, "A new approach for power losses evaluation of IGBT/diode module," *Electronics (Switzerland)*, vol. 10, no. 3, pp. 1–21, 2021, doi: 10.3390/electronics10030280.

[29] G. I. Hasyim, S. Wijanarko, J. Furqani, A. Rizqiawan, and P. A. Dahono, "A current control method for bidirectional multiphase DC-DC boost-buck converter," *International Journal of Electrical and Computer Engineering*, vol. 12, no. 3, pp. 2363–2377, 2022, doi: 10.11591/ijece.v12i3.pp2363-2377.

BIOGRAPHIES OF AUTHORS

Sulistyo Wijanarko 🆔 📇 SC 🔗 received his bachelor's degree in electrical engineering from Universitas Gadjah Mada, in 2013. At present, he is a graduate student at Institut Teknologi Bandung and a research assistant at National Research and Innovation Agency, Indonesia. His field of research is power electronics and drives. He can be contacted at email: suli013@brin.go.id.

Gifari Iswandi Hasyim received his bachelor's degree in electrical power engineering from Institut Teknologi Bandung, in 2020. His field of research is power electronic. At present, he is a graduate student at Institut Teknologi Bandung. He can be contacted at email: gifarihasyim@gmail.com.

Jihad Furqani was born in Malang, East Java, Indonesia in 1990. He received B.S. degree in electrical power engineering from Bandung Institute of Technology in 2012. He received M.S. degree in electrical engineering from Bandung Institute of Technology in 2013. He received Dr. Eng. degree in electrical and electronic engineering from Tokyo Institute of Technology in 2019. He has been studying multilevel and multiphase motor drive, noise reduction in switched reluctance motor, power electronic converter for renewable energy application, and electric motor for vehicle application. He was visiting researcher of University of Akron in 2017 and Visiting Lecture of Tokyo Institute of Technology in 2021. Currently, he is a lecturer in electrical power engineering, school of electrical engineering and informatics, national center for sustainable transportation technology, and center for instrument technology and automation, Bandung Institute of Technology. He received IEEE Star Reviewer in 2019. He can be contacted at email: j.furqani@konversi.ee.itb.ac.id.

Arwindra Rizqiawan received his bachelor and master's degree from Insititut Teknologi Bandung, Indonesia, in 2006 and 2008, respectively, and doctoral degree from Shibaura Institute of Technology, Japan, in 2012, all in the field of electrical engineering. His current main interests are power engineering, power electronics, and renewable energy. He is currently serving as assistant professor in School of Electrical Engineering and Informatics, Institut Teknologi Bandung, Indonesia. He is a certified professional engineer (IPM) in Indonesia by the Institution of Engineers Indonesia (PII), and ASEAN Engineer by ASEAN Engineering Register. He can be contacted at email: windra@staff.stei.itb.ac.id.

Pekik Argo Dahono got the Insinyur (Ir) degree, from the Institut Teknologi Bandung, Indonesia, in 1985, the master and doctor engineering degrees from Tokyo Institute of Technology, Japan, in 1992 and 1995, respectively, all in electrical engineering. He is registered as a professional engineer in Indonesia and ASEAN. He is a senior member of IEEE. He is a cofounder of Indonesia Smart Grid Initiatives and Indonesia Power Quality Initiatives. At present, he is a professor in the School of Electrical Engineering and Informatics, Institut Teknologi Bandung. He has interest in power electronics, power systems, and power quality. He can be contacted at email: pekik@konversi.ee.itb.ac.id.

Anwar Muqorobin studied Electrical Engineering at Universitas Diponegoro and Institut Teknologi Bandung. At present, he is a researcher at Badan Riset dan Inovasi Nasional (BRIN). His research activities are focused on inverter, dc-dc converter and control applications. He can be contacted at email: anwa014@brin.go.id.